

Efficient Spectrum Reshaping with Photonic Gauge Potentials in Resonantly Modulated Fiber-Loop Circuits

Lu Ding,¹ Chengzhi Qin,¹ Feng Zhou,^{1,4} Liu Yang,² Wenwan Li,¹ Fengguang Luo,² Jianji Dong,¹ Bing Wang^{1,*}, and Peixiang Lu^{1,3}

¹ Wuhan National Laboratory for Optoelectronics and School of Physics, Huazhong University of Science and Technology, Wuhan 430074, China

² School of Optical and Electronic Information, Huazhong University of Science and Technology, Wuhan 430074, China

³ Hubei Key Laboratory of Optical Information and Pattern Recognition, Wuhan Institute of Technology, Wuhan 430205, China

⁴ School of Information Science and Engineering & Institute for Advanced Optics, Hunan Institute of Science and Technology, Yueyang 414006, China

(Received 19 April 2019; revised manuscript received 24 June 2019; published 14 August 2019)

We investigate theoretically and experimentally the efficient control of the light spectrum in a fiber-loop circuit with two incorporated phase modulators (PMs). By varying the modulation phases in the PMs, photonic gauge potentials can be introduced in the loop, enabling full control of spectrum shift and band width. The spectrum evolution also depends rigorously on the resonant modulation condition, which suggests that the time delay of light in one circulation equals integer multiples of the modulation period such that the gauge potentials remain constant in distinct circulations. As the two PMs possess the same gauge potentials under resonant conditions, a 50-GHz frequency shift and three-fold band expansion are experimentally realized. For the out-of-phase modulation under resonant conditions, we also achieve the frequency analogue of perfect imaging for arbitrarily input spectra. As the resonant condition is broken, both the spectrum shift and band width are dramatically suppressed. This study may find potential applications in the spectrum management for both optical communications and signal processing.

DOI: 10.1103/PhysRevApplied.12.024027

I. INTRODUCTION

Frequency control such as manipulating the shift and shape of a frequency spectrum has enabled a wide range of applications. A larger frequency shift helps to match the frequency gap between quantum systems and increase the channel capacity of quantum communications, leading to prospective applications in quantum information processing and networking [1–6]. By expanding the spectrum band width, one also can boost the capacity and speed of optical communications [7–11]. After all, the frequency spectrum contains abundant physical information and has been widely exploited in precise optical metrologies and spectroscopies [12–18]. Conventional methods to manipulate the spectrum rely on nonlinear optical effects, such as the sum- or difference-frequency process and four-wave mixing [19–22]. A drawback of nonlinear approaches is the required high pump power to induce efficient frequency conversion [23]. To overcome this limitation, recent efforts have been dedicated

to time-modulation methods, such as electro-optic modulations [24–27], acousto-optic modulations [28–31], and optomechanical vibrations [32–34]. Nevertheless, the conversion efficiency of time modulation is still hindered by the finite modulation depth, which, in turn, limits the ability to manipulate the spectrum. To improve the conversion efficiency, a straightforward way is to utilize more modulators arranged in parallel and/or cascade configurations in order to increase the effective modulation depths. However, this scheme will inevitably increase the system complexity and operation difficulty in synchronizing the modulators.

It was recently revealed that the phase of time modulation is associated with an effective gauge potential for photons [35,36]. The gauge potential can impose an additional phase factor to the photon wave function, analogous to how the electromagnetic vector potential affects the electron wave function [31,35–42]. The gauge potential provides an alternative mechanism to control light propagation in real space, such as realizing one-way edge states [35,43–46] and nonreciprocal light transmission [38–42]. Moreover, it is also possible to create gauge potentials in frequency space by controlling the modulation phases in

*wangbing@hust.edu.cn

optical phase modulators (PMs). The frequency domain gauge potentials can be used to control the frequency analogues of diffraction and refraction, providing an alternative approach to manipulate the spectrum of light [25,47–50]. However, the spectrum manipulation based on gauge potentials is still limited by the low modulation depths due to the single pass of light through the PMs.

The fiber-loop configurations with phase and intensity modulators have been proposed to improve the efficiency of spectrum manipulation and find applications in generating flat and broadband frequency combs [51–53]. Here, we design a fiber-loop circuit with a tunable loop length and incorporate two PMs in the loop such that the gauge potential can be introduced in the system. Furthermore, the modulation efficiency is remarkably enhanced in the loop configuration. By turning the loop length, we can achieve the resonant condition such that light undergoes constructive phase modulations with constant gauge potentials from one circulation to another. Such resonant modulation can increase the effective modulation depths in the two PMs, giving rise to a larger spectrum shift and band-width expansion compared to a single-pass phase modulation. Moreover, as the two PMs in the fiber loop undergo out-of-phase modulations, we can also achieve perfect reconstruction for an arbitrarily input spectrum. Furthermore, we experimentally verify that, as the resonant condition is broken, the spectrum manipulation efficiency will dramatically decrease, giving rise to the suppression of spectrum shift and band expansion. This study applies the concepts of photonic gauge potentials and resonant modulation condition to the manipulation of the light spectrum, which may find applications in spectrum management for optical communications and signal processing.

II. THEORETICAL MODEL

A schematic diagram of a dynamically modulated fiber loop is shown in Fig. 1(a), which comprises two incorporated PMs and a tunable time delay line (TDL) in the loop. The input light can couple into and out of the loop through a directional coupler. The PMs (PM1 and PM2) are modulated by sinusoidal radio frequency (rf) signals with the same modulation frequency Ω , but generally different modulation depths m_1, m_2 and phases ϕ_1, ϕ_2 . Here, two PMs are utilized to enhance the modulation and provide more flexibility to control the frequency spectrum. As the modulation depths and phases are tunable in two PMs, the output spectrum could have a greater variety of evolution processes than that in the loop with only one PM. The output spectrum will be reshaped through multiple phase modulations as light circulates in the loop. As shown in Fig. 1(b), the process of phase modulation can be equivalently described in terms of photonic transitions in a frequency lattice with $\omega_n = \omega_0 + n\Omega$ ($n = 0, \pm 1, \pm 2, \dots$). The modulation frequency and depth correspond to the lattice constant and hopping strength between adjacent lattice sites. It has been recently revealed that the modulation phase ϕ (ϕ_1 or ϕ_2) is associated with an effective gauge potential in the frequency lattice, which can induce a non-reciprocal phase shift of $\pm\phi$ during photonic transitions [25,47,48]. The spectrum evolution in the PMs can thus be manipulated by the gauge potentials through controlling the modulation phases. The notation of gauge potential in the loop circuit is the same as that in a single-pass circuit.

Since the PMs are incorporated in the fiber loop where light can pass through multiple times, the loop length will also have influence on the spectrum evolution. For quantitative analysis, we denote τ as the delay time for light to

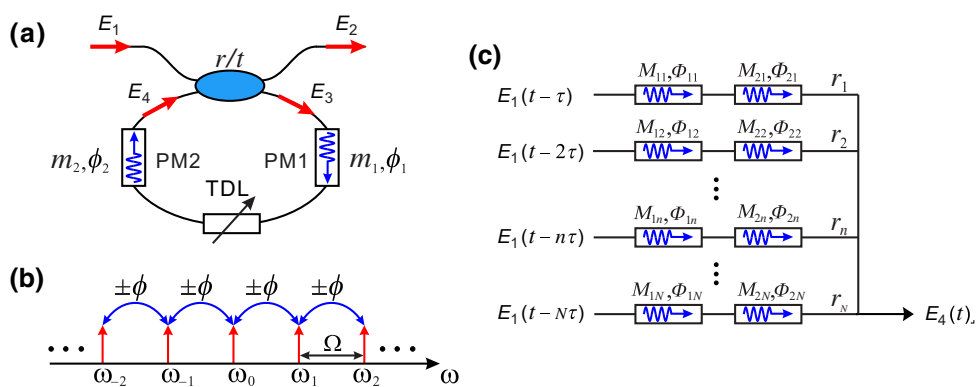


FIG. 1. (a) Schematic sketch of a fiber loop with two phase modulators (PM1 and PM2) and a tunable time delay line (TDL). m_1, m_2 and ϕ_1, ϕ_2 denote the modulation depths and phases of the two PMs. E_1 – E_4 represent the field amplitudes at different ports. The input light couples into and out of the loop through a directional coupler with coupling ratio r^2/t^2 . (b) Nonreciprocal phase shift of ϕ and $-\phi$ during upward and downward transitions. (c) Parallel optical circuits equivalent to the loop circuit shown in (a). M_{jn} and Φ_{jn} are effective modulation depths and phases given by Eqs. (4) and (5), where $j = 1, 2$ denotes PM1 and PM2, $n = 1, 2, \dots, N$ with N being the total circulation times in the loop.

accomplish a complete circulation in the loop. In practice, the delay time can be continuously tuned by the incorporated TDL. For a general choice of loop length, the delay time and modulation frequency obey the following equation

$$\Omega\tau = 2q\pi + \theta, \quad (1)$$

where q is an integer and θ represents the modulation phase shift and equals the deviation of the gauge potential between adjacent circulations. Specifically, with θ as an integer multiple of 2π , the light will experience a constant modulation phase in each circulation, indicating the constructive phase modulation in the loop. Thereafter, we denote this situation as the resonant modulation condition. While for θ not an integer multiple of 2π , the light should undergo a linear shift of modulation phase as the circulation time increases, which is referred to as the off-resonance modulation condition. Generally, the electrical field components at different ports of the coupler can be linked by the following equations

$$\begin{cases} E_2(t) = rE_1(t) + itE_4(t), \\ E_3(t) = itE_1(t) + rE_4(t), \\ E_4(t) = e^{im_2 \cos[\Omega(t-\tau)+\phi_2]} e^{im_1 \cos[\Omega(t-\tau)+\phi_1]} E_3(t-\tau), \end{cases} \quad (2)$$

where r^2/t^2 is the coupling ratio of the directional coupler. $E_1(t)$ and $E_2(t)$ denote the electrical fields at the input and output ports. $E_3(t)$ and $E_4(t)$ represent the electrical fields before and after the PMs in the fiber loop, respectively. From Eq. (2), we can obtain the relation between the input and output fields (see the Appendix)

$$E_2(t) = rE_1(t) - \sum_{n=1}^N r_n^2 e^{iM_{2n} \cos(\Omega t + \Phi_{2n})} e^{iM_{1n} \cos(\Omega t + \Phi_{1n})} \times E_1(t - n\tau). \quad (3)$$

The total output field is the superposition of each output contribution, which has circulated n times in the loop. Here, $n = 1, 2, \dots, N$, with N being the total number of circulation times. The corresponding weight coefficient is $r_n^2 = t^2 r^{(n-1)}$. As shown in Fig. 1(c), the process of light circulation in the loop for n times is equivalent to the process of a single phase modulation, with the effective modulation depths and phases given by (see the Appendix)

$$M_{jn} = \begin{cases} nm_j, & (\theta = 0) \\ \frac{\sin(n\theta/2)}{\sin(\theta/2)} m_j, & (\theta \neq 0) \end{cases} \quad (4)$$

$$\Phi_{jn} = \phi_j - \frac{1}{2}(n+1)\theta, \quad (5)$$

where $j = 1, 2$ denote PM1 and PM2, respectively. Specifically, for the resonant modulation condition $\theta = 0$, the

light will experience a constant gauge potential with a fixed modulation phase $\Phi_{jn} = \phi_j$ ($j = 1, 2$) in each circulation. As a result, these n times of circulation give rise to a modulation depth of nm_j . On the other hand, for the off-resonance condition, the gauge potential exhibits a linear shift as n increases. The modulation depth becomes $\sin(n\theta/2)/\sin(\theta/2)$ times that in a single-pass circuit. In fact, the loop circuit may enhance the modulation as the phase modulators are passed through for many times due to multiple circulations. By adjusting the resonant condition, the phase of the frequency comb in each circulation of the loop can be tunable, providing more flexibility for frequency control.

We first consider the case of inputting a single-frequency light. The incident electrical field is given by $E_1(t) = a_0 \exp(i\omega_0 t)$, where a_0 is the input amplitude. Assume the two PMs possess the same modulation depths $m_1 = m_2$ such that $M_{1n} = M_{2n}$. Substituting the input field into Eq. (3), we can obtain the output electric field

$$E_2(t) = ra_0 e^{i\omega_0 t} - \sum_{s=-\infty}^{\infty} \left\{ (i)^s e^{is(\Phi_{1n} + \Delta\phi/2)} \sum_{n=1}^N r_n^2 \times J_s \left[2M_{1n} \cos\left(\frac{\Delta\phi}{2}\right) \right] \right\} a_0 e^{-in\omega_0 \tau} e^{i(\omega_0 + s\Omega)t}, \quad (6)$$

where $\Delta\phi = \phi_2 - \phi_1$ and s is an integer. The output field can also be written as $E_2(t) = \sum_s a_s \exp[i(\omega_0 + s\Omega)t]$ with a_s being the amplitude at frequency $s\Omega$ and having the form

$$a_s = ra_0 \delta_{s,0} - (i)^s e^{is(\Phi_{1n} + \Delta\phi/2)} \sum_{n=1}^N r_n^2 \times J_s \left[2M_{1n} \cos\left(\frac{\Delta\phi}{2}\right) \right] a_0 e^{-in\omega_0 \tau}. \quad (7)$$

Therefore, as the modulation depths in both PMs are fixed, the output spectrum is only determined by the phase difference of modulation in the two PMs. For other kinds of input light, the output spectrum can be obtained by performing Fourier transformation using the time-varying output electric field in Eq. (3). For example, if we input a frequency comb instead of a single frequency into the system, the output spectrum will also manifest as a frequency comb with the profile being reshaped by the phase modulations in the fiber loop. The theoretical deduction of the output spectrum is provided in the Appendix.

To quantitatively show the spectrum manipulation efficiency, we compare the spectrum evolutions in the loop circuit with two PMs to those in a single-pass one. In the calculation, we vary the total modulation depth m ($=m_1 + m_2$) linearly in the two situations. The coupling ratio is fixed as $r^2/t^2 = 50/50$. The input frequency is

$\omega_0/2\pi = 193.5$ THz, corresponding to $\lambda_0 = 1.55 \mu\text{m}$. The modulation frequency is $\Omega/2\pi = 10$ GHz and the resonant modulation condition is satisfied. Figures 2(a) and 2(b) show the frequency comb generations under a single-frequency light input in the single-pass and the fiber-loop systems, respectively. As $m = 2$, the fiber-loop system can generate a total of 33 comb teeth, which is three times larger than the single-pass system. Thus, the fiber loop can remarkably increase the band width of the frequency comb. In Figs. 2(c) and 2(d), we input a frequency comb with a Gaussian envelope into the two systems. The initial Bloch momentum $\phi_0 - \phi_1 = -\pi/2$ and Gaussian width $W = 5\Omega$. In both situations, the frequency combs experience a blue shift as the modulation depth increases. In the single-pass circuit, the center of the spectrum undergoes a blue shift of 2Ω while the shift becomes 6Ω when the loop is employed. At the same time, the comb width has been increased by 2.5 times. Comparably, the comb width in the single-pass circuit almost remains constant. The reason lies in the uniform direction of group velocity around $\phi_0 - \phi_1 = -\pi/2$ [25]. Concerning the loop circuit, the final output spectrum derives from the superposition of the spectrum in each circulation. The spectra may experience coherent interference as the PMs will modulate the phase of the frequency comb in each circulation of the loop, resulting in the deformation of the spectrum, as shown in Fig. 2(d). Note that the intensity of the spectrum becomes gradually lower as the circulation times increase. It is the spectra passing through the first several circulations of the loop that will largely contribute to the output spectrum.

III. EXPERIMENTAL RESULTS AND DISCUSSIONS

The experimental setup is shown in Fig. 3, which comprises a fiber-loop circuit with two incorporated LiNbO₃ PMs. The fiber loop is excited by using a continuous laser or mode-locked laser through a 50/50 optical fiber coupler. The two PMs (EOSPACE, 12.5+ Gb/s) are identical with a half voltage of $V_\pi \sim 4.9$ V, which are driven by the radio frequency (rf) signals with fixed modulation frequency $\Omega/2\pi = 10$ GHz. In the rf circuit, the rf phase shifters (Weinschel 981) and rf attenuators (Narda 4745-69) are employed to adjust the modulation phases and depths of the two PMs, respectively. The phase difference between the mode-locked laser and the two PMs can be continuously tuned by the rf phase shifter PS0. The modulation phase difference of the two PMs is varied by PS1 and PS2. The modulation depths of the two PMs are controlled by the tunable rf attenuators (VA1, VA2) and rf amplifiers (EA1, EA2). In the optical circuit, a programmable band-pass filter (Finisar 1000S) is utilized to reshape the initial spectrum profile to form a Gaussian envelope. A fiber connector *A* or *B* is used for choosing the continuous or mode-locked laser. In the fiber loop, a TDL is applied to fulfill the resonant modulation condition. Two polarization controllers (PCs) are used to control light polarization states in the PMs. The erbium-doped fiber amplifier (EDFA) and the variable optical attenuator (VOA) are used to control the insertion loss. The output spectrum is detected by the optical spectrum analyzer.

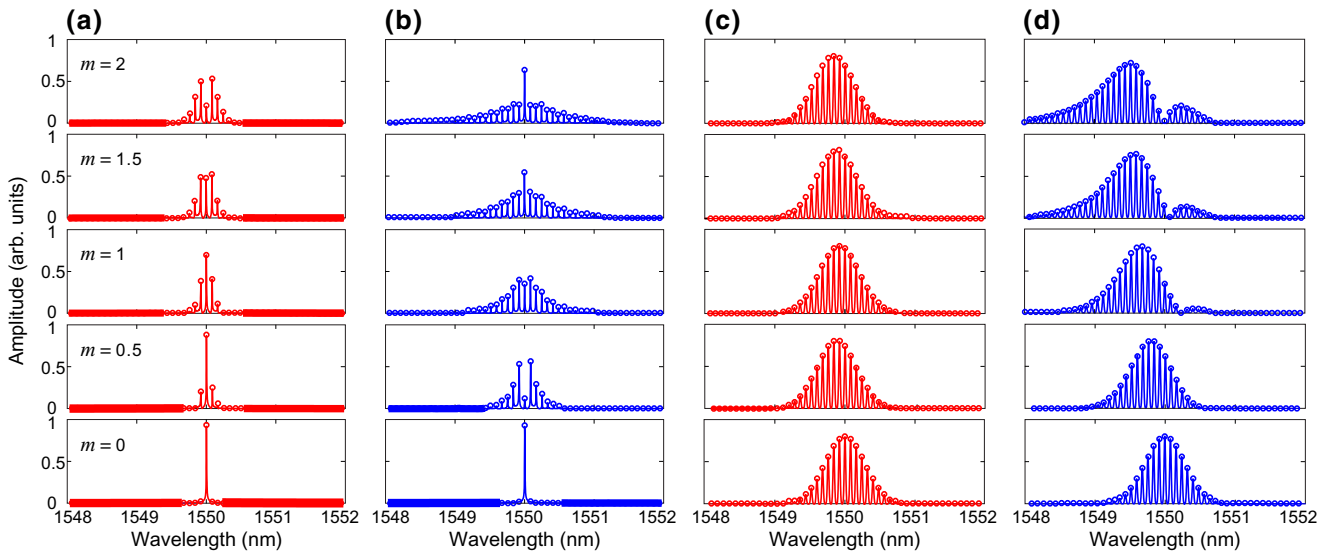


FIG. 2. (a),(b) Spectrum evolutions in two cascaded PMs of a single passage (a) and in the fiber loop (b) for incidence of a single frequency as the total modulation depth increases from $m = 0$ to 2. Here $\Omega/2\pi = 10$ GHz, $\lambda_0 = 1.55 \mu\text{m}$, $\theta = 0$, $\phi_1 = \phi_2$. (c),(d) Corresponding spectrum evolutions for incidence of frequency comb with a Gaussian envelope. The width of the frequency comb is $W = 5\Omega$ and $\phi_0 - \phi_1 = -\pi/2$.

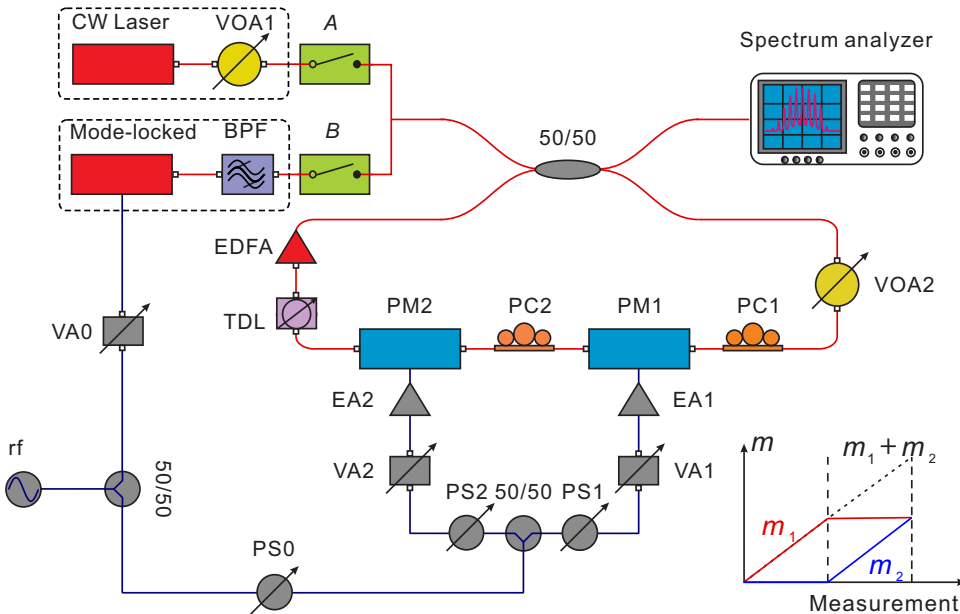


FIG. 3. Schematic diagram of the experimental setup. BPF, band-pass filter; EDFA, erbium-doped fiber amplifier; VOA, variable optical attenuator; PC, polarizer controller; TDL, tunable optical delay line; PS, phase shifter; EA, electrical amplifier; VA, variable attenuator. Mode-locked laser and continuous laser are utilized separately when only one of the fiber connectors *A* or *B* is switched on in each experimental implementation. The inset on the right below shows the way of varying modulation depths m_1 and m_2 of the two PMs. At first, m_1 increases linearly and $m_2 = 0$. Then m_1 is fixed at its maximum and m_2 increases linearly before reaching its maximum.

First, we consider the spectrum evolution for a single frequency input under the resonance condition. For practical implementation, the fiber connector *A* is switched on to inject the continuous laser light. The resonant condition can be tuned by continuously varying the TDL, which is fulfilled as the output spectrum width reaches maximum. Figures 4(a) and 4(b) show the output spectrum evolutions versus the modulation phase difference $\Delta\phi = \phi_2 - \phi_1$ under equal modulation depths $m_1 = m_2 = 0.9$ in the two PMs. The experimental results agree well with the theoretical analysis of Eq. (A11) (see the Appendix). As the modulation phase difference varies from $\Delta\phi = 0$ to π , the width of the output spectrum should vary from its maximum to its minimum.

Then we fix $\Delta\phi = 0$ and successively increase m_1 and m_2 . The measured output spectrum evolution is shown in Fig. 4(c). The spectrum width increases linearly with the modulation depth $m_1 + m_2$. The amplitude of the spectrum is given by

$$a_s = r a_0 \delta_{s,0} - (i)^s e^{is\phi_1} \sum_{n=1}^N r_n^2 J_s(nm_1 + nm_2) a_0 e^{-in\omega_0\tau}. \quad (8)$$

In the calculation, the modulation depths m_1 and m_2 are measured through an oscilloscope. Although the resonance condition Eq. (1) can be easily satisfied in the experiment by detecting the maximum band expansion, the circulation time of light in the loop τ is hard to determine and has to be fitted according to the experimental data. The theoretical fitted results are shown in Fig. 4(d), which agree well with the experimental data. For out-of-phase modulation

as $\Delta\phi = \pi$, the amplitude of the spectrum is

$$a_s = r a_0 \delta_{s,0} - (i)^s e^{is(\phi_1 + \pi/2)} \sum_{n=1}^N r_n^2 J_s(nm_1 - nm_2) a_0 e^{-in\omega_0\tau}. \quad (9)$$

We have $a_s = r a_0 - \sum_{n=1}^N r_n^2 a_0 e^{-in\omega_0\tau}$ for $s = 0$ and $a_s = 0$ for $s \neq 0$, verifying that the output spectrum contains only the zeroth order when $m_1 = m_2$. The measured spectrum evolution is illustrated in Fig. 4(e). One sees that the input single frequency expands to a wide frequency comb when m_1 increases linearly. Then the spectrum is compressed as m_2 increases and ultimately returns back into a single frequency. The theoretical fitted results are shown in Fig. 4(f), which also coincide well with the experimental data. The effect shows perfect imaging of the frequency and may find great applications in optical communications and information processing.

Furthermore, we investigate the spectrum evolution for incidence of a frequency comb. By switching on the fiber connector *B*, we can inject a frequency comb into the fiber loop generated from the mode-locked laser. A band-pass filter (BPF) is used to modulate the frequency comb with a Gaussian envelope. The initial Bloch momentum of the frequency comb is denoted as ϕ_0 . In the experiments, we first fix $\phi_1 = \phi_2$ and $m_1 = m_2 = 1.1$ for the two PMs and continuously vary the phase shifter PS0 to change the modulation phase difference $\phi_0 - \phi_1$. The experimental output spectrum evolution versus $\phi_0 - \phi_1$ is shown in Fig. 5(a). The center of the spectrum envelope manifests a periodical oscillation as the phase difference varies. The analytical results according to Eq. (A14) are shown in

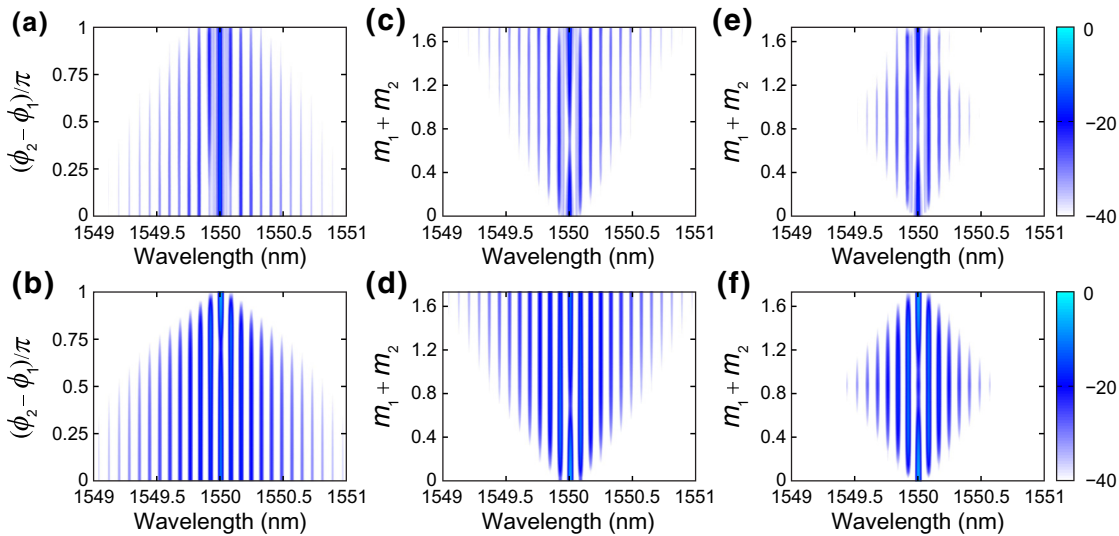


FIG. 4. (a) Experimental and (b) simulated spectrum evolutions versus the phase difference $\phi_2 - \phi_1$ for $m_1 = m_2 = 0.9$ and $\theta = 0$. (c) Experimental and (d) simulated spectrum evolutions for $\phi_2 - \phi_1 = 0$ and $\theta = 0$. (e) Experimental and (f) simulated spectrum evolutions for $\phi_2 - \phi_1 = \pi$ and $\theta = 0$.

Fig. 5(b). They coincide well with the experimental data. The center position of the frequency comb is depicted in Fig. 5(c). Both the experimental and theoretical results show that the spectrum reaches the maximum red and blue shifts of approximately 50 GHz (approximately 0.4 nm) as $\phi_0 - \phi_1 = \pm\pi/2$. At the same time, the bandwidth of the frequency comb varies between 0.52 and 0.67 nm, as shown in Fig. 5(d). As $\phi_0 - \phi_1 = \pi$, the spectral shift vanishes and the band width returns to its initial value. For $\phi_0 - \phi_1 = -\pi/2$, the spectrum evaluation is shown in Fig. 5(e) as $\phi_2 - \phi_1$ varies from 0 to 3π . The results can also be predicted by the theoretical calculation, which is shown in Fig. 5(f). The center position of the frequency comb envelope also experiences periodic oscillations with $\phi_2 - \phi_1$, but with the opposite phase compared with the case of varying $\phi_0 - \phi_1$. As $\phi_2 - \phi_1 = 0$, both the spectrum shift and band width reach their maxima, as shown in Figs. 5(g) and 5(h). The maximum spectrum shift is approximately 50 GHz (approximately 0.4 nm) and the spectrum band width increases from 0.48 to 0.66 nm. As $\phi_2 - \phi_1 = \pm\pi$, the output spectrum remains unchanged with respect to the input spectrum, manifesting the perfect imaging for the input frequency comb.

The frequency shift in the loop can be qualitatively explained by the band structure of a single-pass circuit with PMs [25]. The frequency comb is regarded as a Bloch mode in the frequency lattice created by the phase modulators, where the band structure follows a sinusoidal curve. As the incident Bloch momentum $\phi_0 - \phi_1$ reverses its sign, the group velocity will also change direction in the frequency dimension, resulting in a red or blue shift for the frequency comb with a finite width. Under resonant condition, the Bloch momenta of the frequency combs in

different circulations of the loop are equivalently valued. Consequently, all the combs have to experience a uniform red or blue shift. Since the final output spectrum is obtained by the superposition of the frequency combs in all circulations, it will undergo a blue or red shift just as that in a single-pass circuit.

To explore the spectrum evolution for specific gauge potentials, we fix the modulation phases in the PMs and increase the corresponding modulation depths m_1 and m_2 . First, we choose the same gauge potentials in the two PMs such that $\phi_1 = \phi_2$. The increase of the effective modulation depths is implemented according to the scheme shown in the inset of Fig. (3). Figures 6(a) and 6(b) illustrate the spectrum evolutions versus the total modulation depth $m_1 + m_2$ for a frequency comb input as $\phi_0 - \phi_1 = -\pi/2$ and $\pi/2$. The spectra manifest blue and red shifts, respectively. The maximum shift of the spectral envelope reaches approximately 50 GHz (approximately 0.4 nm), covering more than five comb lines. Meanwhile, the width of the spectrum in both cases is broadened by three times as the modulation depth increases. For $\phi_0 - \phi_1 = 0$, as shown in Fig. 6(c), the shift of the spectral envelope vanishes, but the width is still remarkably expanded. In Fig. 6(d), we choose different gauge potentials in the two PMs as $\phi_0 - \phi_1 = -\pi/2$ and $\phi_0 - \phi_2 = \pi/2$. The input frequency comb experiences a blue shift and expansion at first and then the process is reversed until the spectrum returns to its origin. The theoretical calculation is performed by solving Eq. (3) under a frequency comb input. The details are provided in Eqs. (A15) and (A16) of the Appendix. The simulated results are shown in Figs. 6(e)–6(h), which agree fairly well with the experimental data.

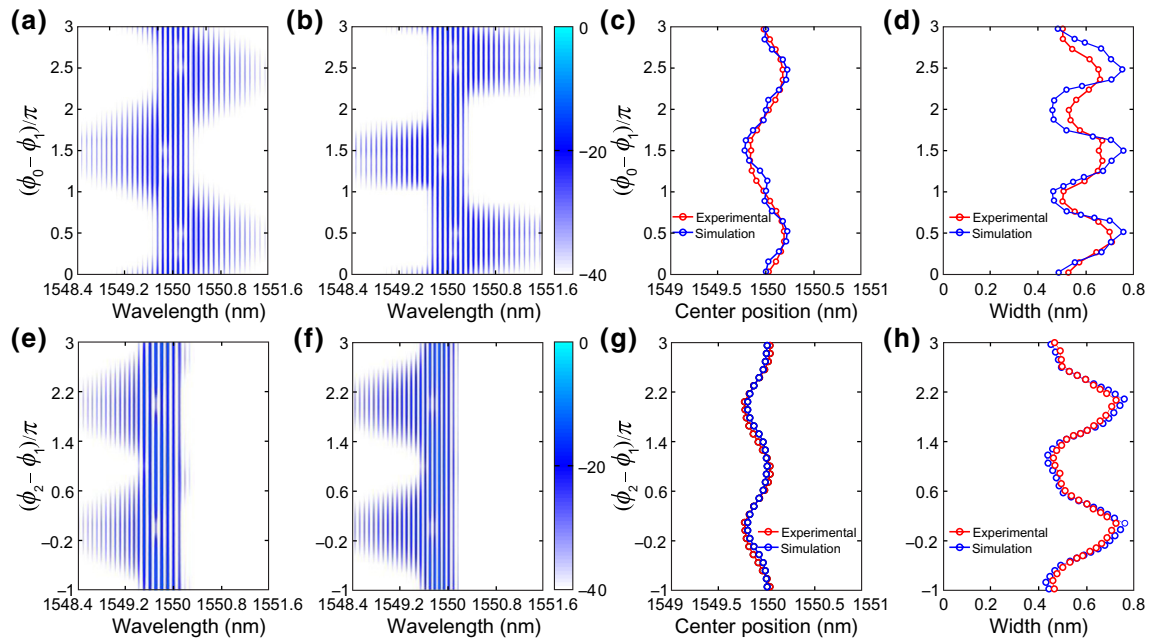


FIG. 5. (a) Experimental and (b) simulated spectrum evolutions versus the phase difference $\phi_0 - \phi_1$ for $\phi_1 = \phi_2$, $\theta = 0$, and $m_1 = m_2 = 1.1$. (c) Center position of the frequency comb as a function of $\phi_0 - \phi_1$. The red and blue circles indicate the experimental and theoretical results. (d) Band width of the frequency comb as a function of $\phi_0 - \phi_1$. (e) Experimental and (f) simulated spectrum evolutions versus the phase difference $\phi_2 - \phi_1$ for $\phi_0 - \phi_1 = -\pi/2$. Other parameters are kept the same as those in (a) and (b). (g) Center position of the frequency comb as a function of $\phi_2 - \phi_1$. (h) Band width of the frequency comb as a function of $\phi_2 - \phi_1$.

All of the above results are based on the resonant modulation condition with constant gauge potentials in the PMs. Now we consider the off-resonance condition as θ varies when the gauge potentials experience a linear shift as the circulation time increases. Figure 7(a) shows the output spectrum evolution under a single frequency input as the detuned phase θ varies. Here, the modulation

depths $m_1 = m_2$ and the initial modulation phases $\phi_1 = \phi_2$ in the two PMs. The output frequency comb undergoes a remarkable expansion in band width under the resonant modulation condition. For the off-resonant condition, the width of the frequency comb is largely suppressed. The theoretical results are shown in Fig. 7(b), which agrees well with the experimental data. Figure 7(c) illustrates the

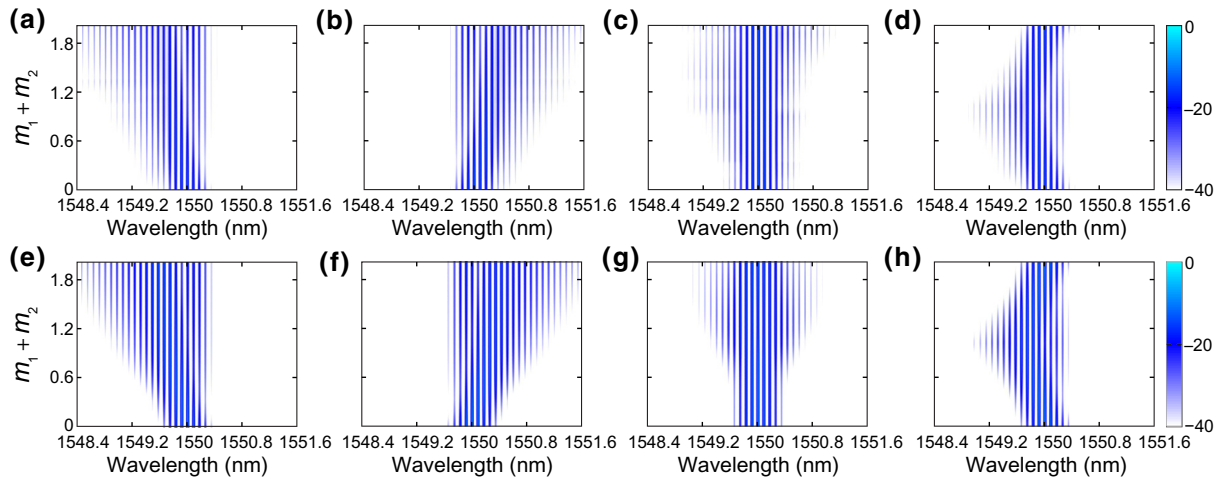


FIG. 6. (a)–(c) Experimental spectrum evolutions for $\phi_0 - \phi_1 = -\pi/2$, $\pi/2$, and 0, respectively. Here, $\phi_1 = \phi_2$ and the resonant modulation condition is satisfied. (d) Experimental spectrum evolutions for $\phi_0 - \phi_1 = -\pi/2$ and $\phi_0 - \phi_2 = \pi/2$. (e)–(h) Simulated results corresponding to (a)–(d).

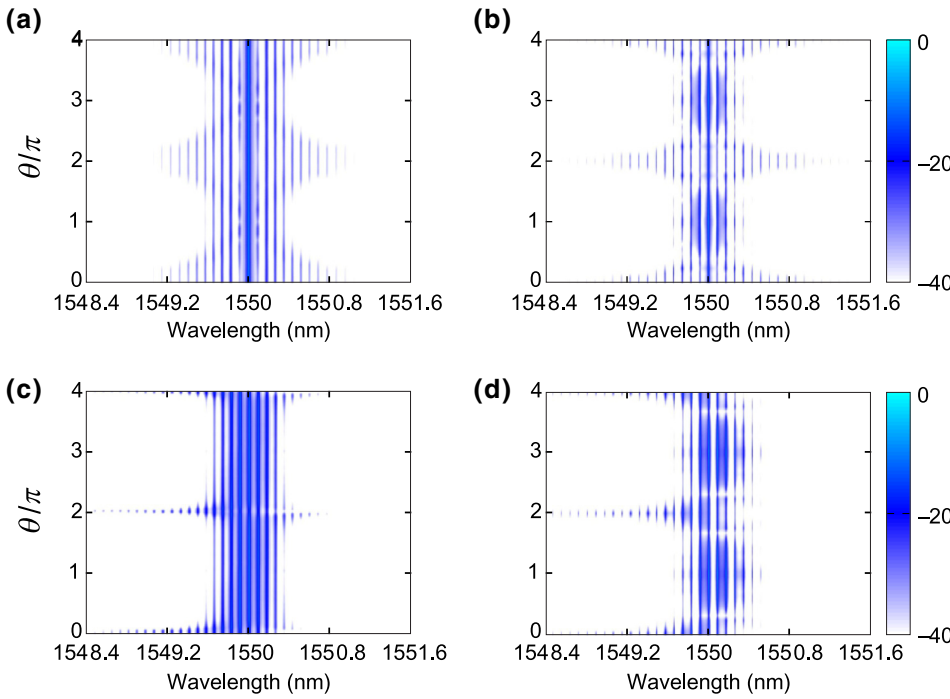


FIG. 7. (a) Experimental and (b) simulated results of spectrum evolutions as θ varies for single-frequency input. Here, $\phi_1 = \phi_2$ and $m_1 = m_2 = 0.9$. (c) Experimental and (d) simulated results of spectrum evolution as θ varies for frequency comb input. Here, $\phi_0 - \phi_1 = -\pi/2$, $\phi_1 = \phi_2$, and $m_1 = m_2 = 1.1$.

measured evolution of the output spectrum with the variation of θ for the input of the frequency comb. One sees that the spectrum shift and band expansion both reach the maxima as θ reaches an integer multiple of 2π , while it dramatically decreases for other values. The experimental data are predicted well by the theoretical computations shown in Fig. 7(d). The results can be explained as follows. In the n th circulation of the loop, the shift of the spectrum is given by $|\Delta\omega| = |\sin(n\theta/2)/\sin(\theta/2)|m\Omega$. As the circulation time n increases, a very small θ around an integer multiple of 2π will cause a large frequency shift. The spectrum modulation in the loop is quite sensitive to the resonant condition. The dramatic expansion of the spectrum under the resonant condition should be attributed to higher-order circulations in the loop.

IV. CONCLUSIONS

In summary, we demonstrate efficient manipulation of the light spectrum using photonic gauge potentials in a resonant-modulated fiber-loop circuit with two incorporated PMs. The gauge potentials are introduced by controlling the modulation phases in the PMs and the resonant condition is controlled by tuning the length of the fiber loop. Under the resonant modulation condition, we achieve a maximum spectrum shift of up to 50 GHz and a bandwidth expansion up to three fold for the frequency comb input. As the two PMs are under out-of-phase modulation, we also realize spectrum perfect imaging for both single frequency and frequency comb inputs. As the resonant

condition is broken, the efficiency of spectrum manipulation will decrease dramatically, giving rise to the suppression of spectrum shifting and band-width expansion. The study reveals the significance of resonant condition in the control of spectrum evolution in time-modulated circuits, which may find applications in spectrum and signal reshaping and management for both optical communications and information processing.

ACKNOWLEDGMENTS

The work is supported by the National Natural Science Foundation of China (Grant No. 11674117). C.Q. acknowledges financial support from Boxin project (Grant No. BX20190129). L.D. thanks Yuan Yu and Ning Yang for the useful discussions and help in the experiment.

L.D. and C.Q. contributed equally to this work.

APPENDIX: DERIVATION OF THE LOOP OUTPUT ELECTRICAL FIELD

Here, we provide the detailed derivation of the input-output relation of Eq. (3) in the main text. The original iterative equations read as follows

$$\begin{cases} E_2(t) = rE_1(t) + itE_4(t), \\ E_3(t) = itE_1(t) + rE_4(t), \\ E_4(t) = e^{im_2 \cos[\Omega(t-\tau)+\phi_2]} e^{im_1 \cos[\Omega(t-\tau)+\phi_1]} E_3(t-\tau), \end{cases} \quad (A1)$$

which gives rise to the input-output relation

$$E_2(t) = rE_1(t) - t^2 \sum_{n=1}^N r^{n-1} e^{im_1 F_n(\Omega t)} e^{im_2 G_n(\Omega t)} E_1(t - n\tau), \quad (\text{A2})$$

where $F_n(\Omega t)$ and $G_n(\Omega t)$ are given by

$$\begin{cases} F_n(\Omega t) = \sum_{k=1}^n \cos(\Omega t - k\theta + \phi_1), \\ G_n(\Omega t) = \sum_{k=1}^n \cos(\Omega t - k\theta + \phi_2). \end{cases} \quad (\text{A3})$$

For the resonant modulation condition $\theta = 0$, we have

$$E_2(t) = rE_1(t) - t^2 \sum_{n=1}^N r^{n-1} e^{inm_1 \cos(\Omega t + \phi_1)} e^{inm_2 \cos(\Omega t + \phi_2)} \times E_1(t - n\tau). \quad (\text{A4})$$

For the off-resonance condition $\theta \neq 0$, by using Chebyshev polynomials of the first kind $T_k(\cos\theta) = \cos(k\theta)$ and the second kind $U_{k-1}(\cos\theta) = \sin(k\theta)/\sin\theta$, Eq. (A3) can be simplified as

$$\begin{aligned} F_n(\Omega t) &= \cos(\Omega t + \phi_1) \sum_{k=1}^n T_k(\cos\theta) + \sin\theta \sin(\Omega t + \phi_1) \sum_{k=1}^n U_{k-1}(\cos\theta) \\ &= \frac{1}{2} \cos(\Omega t + \phi_1) \sum_{k=1}^n (e^{i\theta k} + e^{-i\theta k}) - \frac{i}{2} \sin(\Omega t + \phi_1) \sum_{k=1}^n (e^{i\theta k} - e^{-i\theta k}) \\ &= \frac{1}{2} \cos(\Omega t + \phi_1) \left[\frac{e^{i\theta} - e^{i(n+1)\theta}}{1 - e^{i\theta}} + \frac{e^{-i\theta} - e^{-i(n+1)\theta}}{1 - e^{-i\theta}} \right] - \frac{i}{2} \sin(\Omega t + \phi_1) \left[\frac{e^{i\theta} - e^{i(n+1)\theta}}{1 - e^{i\theta}} - \frac{e^{-i\theta} - e^{-i(n+1)\theta}}{1 - e^{-i\theta}} \right] \\ &= \frac{1}{2} e^{-i(\Omega t + \phi_1)} \left(\frac{e^{i\theta} - e^{i(n+1)\theta}}{1 - e^{i\theta}} \right) + \frac{1}{2} e^{i(\Omega t + \phi_1)} \left(\frac{e^{-i\theta} - e^{-i(n+1)\theta}}{1 - e^{-i\theta}} \right) \\ &= \frac{\sin(n\theta/2)}{\sin(\theta/2)} \cos \left[\Omega t + \phi_1 - \frac{1}{2}(n+1)\theta \right]. \end{aligned} \quad (\text{A5})$$

Similarly, $G_n(\Omega t)$ can be rewritten as

$$G_n(\Omega t) = \frac{\sin(n\theta/2)}{\sin(\theta/2)} \cos \left[\Omega t + \phi_2 - \frac{1}{2}(n+1)\theta \right]. \quad (\text{A6})$$

Denoting $C_n = \sin(n\theta/2)/\sin(\theta/2)$ and substituting Eqs. (A5) and (A6) into (A2), we have

$$\begin{aligned} E_2(t) &= rE_1(t) - t^2 \sum_{n=1}^N r^{n-1} e^{iC_n m_1 \cos[\Omega t - (1/2)(n+1)\theta + \phi_1]} \\ &\quad \times e^{iC_n m_2 \cos[\Omega t - (1/2)(n+1)\theta + \phi_2]} E_1(t). \end{aligned} \quad (\text{A7})$$

Eqs. (A4) and (A7) can thus be written in the unified formula

$$\begin{aligned} E_2(t) &= rE_1(t) \\ &\quad - \sum_{n=1}^N r_n^2 e^{iM_{2n} \cos(\Omega t + \Phi_{2n})} e^{iM_{1n} \cos(\Omega t + \Phi_{1n})} E_1(t - n\tau), \end{aligned} \quad (\text{A8})$$

where $r_n^2 = t^2 r^{(n-1)}$ is a weight coefficient and M_{jn} , Φ_{jn} ($j = 1, 2$) are the effective modulation depths and phases, respectively, which are given by

$$M_{jn} = \begin{cases} nm_j, & (\theta = 0) \\ \frac{\sin(n\theta/2)}{\sin(\theta/2)} m_j, & (\theta \neq 0) \end{cases} \quad (\text{A9})$$

$$\Phi_{jn} = \phi_j - \frac{1}{2}(n+1)\theta. \quad (\text{A10})$$

Consider a single-frequency light signal input with the electrical field $E_1(t) = a_0 \exp(i\omega_0 t)$, where the output field is given by

$$\begin{aligned} E_2(t) &= ra_0 e^{i\omega_0 t} - \sum_{s=-\infty}^{\infty} \left\{ (i)^s e^{is(\Phi_{1n} + \Delta\phi/2)} \sum_{n=1}^N r_n^2 \right. \\ &\quad \times J_s \left[2M_{1n} \cos \left(\frac{\Delta\phi}{2} \right) \right] \left. \right\} a_0 e^{-in\omega_0 \tau} e^{i(\omega_0 + s\Omega)t}. \end{aligned} \quad (\text{A11})$$

Denoting $\Delta\phi = \phi_2 - \phi_1$ and $m_1 = m_2$ such that $M_{1n} = M_{2n}$, the complex amplitude of the output spectrum is

$$a_s = ra_0\delta_{s,0} - (i)^s e^{is(\Phi_{1n} + \Delta\phi/2)} \sum_{n=1}^N r_n^2$$

$$\times J_s \left[2M_{1n} \cos\left(\frac{\Delta\phi}{2}\right) \right] a_0 e^{-in\omega_0\tau}. \quad (\text{A12})$$

Specifically, under in-phase and out-of-phase modulations in the two PMs, the output spectra are

$$a_s = \begin{cases} ra_0\delta_{s,0} - (i)^s e^{is\Phi_{1n}} \sum_{n=1}^N r_n^2 J_s(M_{1n} + M_{2n}) a_0 e^{-in\omega_0\tau}, & (\Delta\phi = 0) \\ ra_0\delta_{s,0} - (i)^s e^{is(\Phi_{1n} + \pi/2)} \sum_{n=1}^N r_n^2 J_s(M_{1n} - M_{2n}) a_0 e^{-in\omega_0\tau}. & (\Delta\phi = \pi) \end{cases} \quad (\text{A13})$$

Similarly, we consider a Gaussian wave packet input with the electrical-field distribution $E_1(t) = \sum_m a_0 \exp[-(m\Omega/W)^2] \exp(im\phi_0) \exp[i(\omega_0 + m\Omega)t]$, where W is the width of the Gaussian envelope and ϕ_0 is the initial Bloch momentum. Denoting $m_1 = m_2$ and $\Delta\phi = \phi_2 - \phi_1$, we have

$$\begin{aligned} a_s = & r \sum_m a_0 e^{-(m\Omega/W)^2} e^{im\phi_0} \delta_{s,m} \\ & - \sum_m (i)^{s-m} e^{i(s-m)(\Phi_{1n} + \Delta\phi/2)} \\ & \times \sum_{n=1}^N r_n^2 J_{s-m} \left[2M_{1n} \cos\left(\frac{\Delta\phi}{2}\right) \right] a_0 e^{-(m\Omega/W)^2} \\ & \times e^{i(m\phi_0 - n\omega_0\tau - mn\theta)}. \end{aligned} \quad (\text{A14})$$

In particular, under in-phase modulation, the output spectrum is

$$\begin{aligned} a_s = & r \sum_m a_0 e^{-(m\Omega/W)^2} e^{im\phi_0} \delta_{s,m} - \sum_m (i)^{s-m} e^{i(s-m)\Phi_{1n}} \\ & \times \sum_{n=1}^N r_n^2 J_{s-m} (M_{1n} + M_{2n}) a_0 e^{-(m\Omega/W)^2} \\ & \times e^{i(m\phi_0 - n\omega_0\tau - mn\theta)}. \end{aligned} \quad (\text{A15})$$

Similarly, under the out-of-phase modulation, the output spectrum is given by

$$\begin{aligned} a_s = & r \sum_m a_0 e^{-(m\Omega/W)^2} e^{im\phi_0} \delta_{s,m} - \sum_m (i)^{s-m} e^{i(s-m)\Phi_{1n}} \\ & \times \sum_{n=1}^N r_n^2 J_{s-m} (M_{1n} - M_{2n}) a_0 e^{-(m\Omega/W)^2} e^{i(m\phi_0 - n\omega_0\tau - mn\theta)}. \end{aligned} \quad (\text{A16})$$

All the above theoretical analysis is verified by the experimental results in Figs. 4–7.

-
- [1] S. Zaske, A. Lenhard, C. A. Keßler, J. Kettler, C. Hepp, C. Arend, R. Albrecht, W. Schulz, M. Jetter, P. Michler, and C. Becher, Visible-to-Telecom Quantum Frequency Conversion of Light from a Single Quantum Emitter, *Phys. Rev. Lett.* **109**, 147404 (2012).
 - [2] M. Karpiński, M. Jachura, L. J. Wright, and B. J. Smith, Bandwidth manipulation of quantum light by an electro-optic time lens, *Nat. Photonics* **11**, 53 (2017).
 - [3] Y. Zhao, Y. Zhou, J. Liang, Z. Zeng, Q. Ke, Y. Liu, M. Li, and P. Lu, Frustrated tunneling ionization in the elliptically polarized strong laser fields, *Opt. Express* **27**, 21689 (2019).
 - [4] S. Ates, I. Agha, A. Gulinatti, I. Rech, M. T. Rakher, A. Badolato, and K. Srinivasan, Two-Photon Interference Using Background-Free Quantum Frequency Conversion of Single Photons Emitted by an InAs Quantum Dot, *Phys. Rev. Lett.* **109**, 147405 (2012).
 - [5] Sören Wengerowsky, Siddarth Koduru Joshi, Fabian Steinlechner, Hannes Hübel, and Rupert Ursin, An entanglement-based wavelength-multiplexed quantum communication network, *Nature* **564**, 225 (2018).
 - [6] Chuan-zhou Zhu, Shimpei Endo, Pascal Naidon, and Peng Zhang, Scattering and bound states of two polaritons in an array of coupled cavities, *Few-Body Syst.* **54**, 1921 (2013).
 - [7] J. Pfeifle, V. Brasch, M. Lauermann, Y. Yu, D. Wegner, T. Herr, K. Hartinger, P. Schindler, J. Li, D. Hillerkuss, R. Schmogrow, C. Weimann, R. Holzwarth, W. Freude, J. Leuthold, T. J. Kippenberg, and C. Koos, Coherent terabit communications with microresonator kerr frequency combs, *Nat. Photonics* **8**, 375 (2014).
 - [8] C. Weimann, P. C. Schindler, R. Palmer, S. Wolf, D. Bekele, D. Korn, J. Pfeifle, S. Koeber, R. Schmogrow, L. Alloatti, D. Elder, H. Yu, W. Bogaerts, L. R. Dalton, W. Freude, J. Leuthold, and C. Koos, Silicon-organic hybrid (SOH) frequency comb sources for terabit/s data transmission, *Opt. Express* **22**, 3629 (2014).
 - [9] R. Hui, B. Zhu, R. Huang, C. T. Allen, K. R. Demarest, and D. Richards, Subcarrier multiplexing for high-speed optical transmission, *J. Lightwave Technol.* **20**, 417 (2002).

- [10] W. Shieh, Q. Yang, and Y. Ma, 107 Gb/s coherent optical OFDM transmission over 1000-Km SSMF fiber using orthogonal band multiplexing, *Opt. Express* **16**, 6378 (2008).
- [11] D. Hillerkuss, et al., 26 Tbit/s line-rate super-channel transmission utilizing all-optical fast Fourier transform processing, *Nat. Photonics* **5**, 364 (2011).
- [12] A. Schliesser, N. Picqué, and T. W. Hänsch, Mid-infrared frequency combs, *Nat. Photonics* **6**, 440 (2012).
- [13] Th. Udem, R. Holzwarth, and T. W. Hänsch, Optical frequency metrology, *Nature* **416**, 233 (2002).
- [14] T. Steinmetz, T. Wilken, C. Araujo-Hauck, R. Holzwarth, T. W. Hänsch, L. Pasquini, A. Manescu, S. D'Odorico, M. T. Murphy, T. Kentischer, W. Schmidt, and T. Udem, Laser frequency combs for astronomical observations, *Science* **321**, 1335 (2008).
- [15] R. Holzwarth, Th. Udem, T. W. Hänsch, J. C. Knight, W. J. Wadsworth, and P. St. J. Russel, Optical Frequency Synthesizer for Precision Spectroscopy, *Phys. Rev. Lett.* **85**, 2264 (2000).
- [16] D. R. Solli, J. Chou, and B. Jalali, Amplified wavelength-time transformation for real-time spectroscopy, *Nat. Photonics* **2**, 48 (2008).
- [17] K. Goda and B. Jalali, Dispersive Fourier transformation for fast continuous single-shot measurements, *Nat. Photonics* **7**, 102 (2013).
- [18] K. Goda, K. K. Tsia, and B. Jalali, Serial time-encoded amplified imaging for real-time observation of fast dynamic phenomena, *Nature* **458**, 1145 (2009).
- [19] J. B. Christensen, J. G. Koefoed, B. A. Bell, C. J. McKinstry, and K. Rottwitt, Shape-preserving and unidirectional frequency conversion by four-wave mixing, *Opt. Express* **26**, 13 (2018).
- [20] B. A. Bell, K. Wang, A. Solntsev, D. N. Neshev, A. A. Sukhorukov, and B. J. Eggleton, Spectral photonic lattices with complex long-range coupling, *Optica* **4**, 11 (2017).
- [21] D. Zhao, S. Ke, Y. Hu, B. Wang, and P. Lu, Optical bistability of graphene embedded in parity-time-symmetric photonic lattices, *J. Opt. Soc. Am. B* **36**, 1731 (2019).
- [22] G. Hu, X. Hong, K. Wang, J. Wu, H. Xu, W. Zhao, W. Liu, S. Zhang, F. Garcia-Vidal, B. Wang, P. Lu, and C. Qiu, Coherent steering of nonlinear chiral valley photons with a synthetic Au–WS₂ metasurface, *Nat. Photonics* **13**, 467 (2019).
- [23] X. Guo, C. L. Zou, H. Jung, and H. X. Tang, On-Chip Strong Coupling and Efficient Frequency Conversion Between Telecom and Visible Optical Modes, *Phys. Rev. Lett.* **117**, 123902 (2016).
- [24] L. J. Wright, M. Karpiński, C. Söller, and B. J. Smith, Spectral Shearing of Quantum Light Pulses by Electro-Optic Phase Modulation, *Phys. Rev. Lett.* **118**, 023601 (2017).
- [25] C. Qin, F. Zhou, Y. Peng, D. Sounas, X. Zhu, B. Wang, J. Dong, X. Zhang, A. Alù, and P. Lu, Spectrum Control through Discrete Frequency Diffraction in the Presence of Photonic Gauge Potentials, *Phys. Rev. Lett.* **120**, 133901 (2018).
- [26] D. Zhao, D. Zhong, Y. Hu, S. Ke, and W. Liu, Imaginary modulation inducing giant spatial Goos–Hänchen shifts in one-dimensional defective photonic lattices, *Opt. Quantum Electron.* **51**, 113 (2019).
- [27] H. Chen, C. Qin, B. Wang, and P. Lu, Discrete refraction and reflection in temporal lattice heterostructures, *Opt. Lett.* **44**, 363 (2019).
- [28] R. Fleury, D. L. Sounas, and A. Alù, Non-reciprocal optical mirrors based on spatio-temporal acousto-optic modulation, *J. Opt.* **20**, 034007 (2018).
- [29] D. M. Kinyua, H. Long, X. Xing, S. Njoroge, K. Wang, B. Wang, and P. Lu, Gigahertz acoustic vibrations of Ga-doped ZnO nanoparticle array, *Nanotechnology* **30**, 305201 (2019).
- [30] R. Fleury, D. L. Sounas, and A. Alù, Subwavelength ultrasonic circulator based on spatiotemporal modulation, *Phys. Rev. B* **91**, 174306 (2015).
- [31] L. Enbang, B. J. Eggleton, K. Fang, and S. Fan, Photonic Aharonov-Bohm effect in photon-photon interactions, *Nat. Commun.* **5**, 3225 (2014).
- [32] K. Fang, J. Luo, A. Metelmann, M. H. Matheny, F. Marquardt, A. A. Clerk, and O. Painter, Generalized non-reciprocity in an optomechanical circuit via synthetic magnetism and reservoir engineering, *Nat. Phys.* **13**, 465 (2017).
- [33] E. Li, B. J. Eggleton, M. Poot, R. Cheng, X. Guo, and H. Tang, Integrated optomechanical single-photon frequency shifter, *Nat. Photonics* **10**, 766 (2016).
- [34] F. Ruesink, M. Miri, A. Alù, and E. Verhagen, Nonreciprocity and magnetic-free isolation based on optomechanical interactions, *Nat. Commun.* **7**, 13662 (2016).
- [35] K. Fang, Z. Yu, and S. Fan, Realizing effective magnetic field for photons by controlling the phase of dynamic modulation, *Nat. Photonics* **6**, 782 (2012).
- [36] K. Fang, Z. Yu, and S. Fan, Photonic Aharonov-Bohm Effect Based on Dynamic Modulation, *Phys. Rev. Lett.* **108**, 153901 (2012).
- [37] D. L. Sounas and A. Alù, Non-reciprocal photonics based on time modulation, *Nat. Photonics* **11**, 774 (2017).
- [38] L. D. Tzuang, K. Fang, P. Nussenzveig, S. Fan, and M. Lipson, Non-reciprocal phase shift induced by an effective magnetic flux for light, *Nat. Photonics* **8**, 701 (2014).
- [39] D. L. Sounas and A. Alù, Angular-momentum-biased nanorings to realize magnetic-free integrated optical isolation, *ACS Photonics* **1**, 198 (2014).
- [40] N. A. Estep, D. L. Sounas, J. Soric, and A. Alù, Magnetic-free non-reciprocity and isolation based on parametrically modulated coupled-resonator loops, *Nat. Phys.* **10**, 923 (2014).
- [41] Z. Yu and S. Fan, Complete optical isolation created by indirect interband photonic transitions, *Nat. Photonics* **3**, 91 (2009).
- [42] Y. Shi, S. Han, and S. Fan, Optical circulation and isolation based on indirect photonic transitions of guided resonance modes, *ACS Photonics* **4**, 1639 (2017).
- [43] L. Yuan and S. Fan, Topologically nontrivial Floquet band structure in a system undergoing photonic transitions in the ultrastrong-coupling regime, *Phys. Rev. A* **92**, 053822 (2015).
- [44] L. Lu, J. D. Joannopoulos, and M. Soljačić, Topological photonics, *Nat. Photonics* **8**, 821 (2014).

- [45] Z. Wang, Y. Chong, J. D. Joannopoulos, and M. Soljačić, Observation of unidirectional backscattering-immune topological electromagnetic states, *Nature* **461**, 772 (2009).
- [46] T. Ozawa, H. M. Price, N. Goldman, O. Zilberberg, and L. Carusotto, Synthetic dimensions in integrated photonics: From optical isolation to four-dimensional quantum Hall physics, *Phys. Rev. A* **93**, 043827 (2016).
- [47] C. Qin, L. Yuan, B. Wang, S. Fan, and P. Lu, Effective electric-field force for a photon in a synthetic frequency lattice created in a waveguide modulator, *Phys. Rev. A* **97**, 063838 (2018).
- [48] C. Qin, Y. Peng, Y. Li, X. Zhu, B. Wang, C. Qiu, and P. Lu, Spectrum Manipulation for Sound with Effective Gauge Fields in Cascading Temporally Modulated Waveguides, *Phys. Rev. Appl.* **11**, 064012 (2019).
- [49] L. Yuan and S. Fan, Bloch oscillation and unidirectional translation of frequency in a dynamically modulated ring resonator, *Optica* **3**, 1014 (2016).
- [50] L. Yuan, Y. Shi, S. Fan, and N. Goldman, Photonic gauge potential in a system with a synthetic frequency dimension, *Opt. Lett.* **41**, 741 (2016).
- [51] K. Ho and J. M. Kahn, Optical frequency comb generator using phase modulation in amplified circulating loop, *IEEE Photon. Technol. Lett.* **5**, 721 (1993).
- [52] S. Bennett, B. Cai, E. Burr, O. Gough, and A. J. Seeds, 1.8-THz bandwidth, zero-frequency error, tunable optical comb generator for DWDM applications, *IEEE Photon. Technol. Lett.* **11**, 551 (1999).
- [53] M. Hirano and A. Morimoto, Generation of flat optical frequency comb by fiber loop modulation, *Opt. Rev.* **18**, 13 (2011).